Solar-Synchronous Tides in Mars Thermosphere CO2, Ar, and N2 Densities From MAVEN

Jeffrey M. Forbes, Xiaoli Zhang, Xiaohua Fang, Mehdi Benna, Francisco González-Galindo, Francois Forget, Ehouarn Millour

JGR Space Physics

RESEARCH ARTICLE
10.1029/2023JA031637

Solar-Synchronous Tides in Mars Thermosphere CO_2, Ar, and N_2 Densities From MAVEN

Jeffrey M. Forbes[1], Xiaoli Zhang[1], Xiaohua Fang[2], Mehdi Benna[3,4], Francisco González-Galindo[5], Francois Forget[6], and Ehouarn Millour[6]

[1]Ann and H.J. Smead Department of Aerospace Engineering Sciences, University of Colorado, Boulder, CO, USA, [2]Laboratory for Atmospheric and Space Physics, University of Colorado, Boulder, CO, USA, [3]Center for Space Sciences and Technology, University of Maryland, Baltimore County, Baltimore, MD, USA, [4]Center for Research and Exploration in Space Science and Technology, NASA Goddard Space Flight Center, Greenbelt, MD, USA, [5]Instituto de Astrofísica de Andalucía, CSIC, Granada, Spain, [6]Institut Polytechnique de Paris, LMD/IPSL, ENS, École Polytechnique, CNRS, Sorbonne Université, Université PSL, Paris, France

Abstract Measurements of CO_2, Ar and N_2 densities from the Neutral Gas and Ion Mass Spectrometer on the Mars Atmosphere and Volatile Evolution Mission (MAVEN) between 150 and 200 km altitude during 2015–2022 are analyzed to reveal diurnal (DW1), semidiurnal (SW2) and terdiurnal (TW3) solar-synchronous tides in Mars thermosphere. Multi-year-mean tidal perturbations on a diurnal- and zonal-mean background, corrected for solar flux variations, are reported as a function of latitude (48°S–48°N), altitude and solar longitude (Ls). The DW1, SW2 and TW3 amplitudes at for example, 180 km altitude are of order 90%–120%, 15%–20%, and $\lesssim$10% for CO_2 and Ar, and roughly 2/3 these values for N_2, the latter presumably due to the difference in molecular weight from the other species. Through examination of vertical phase progressions, DW1 is concluded to be mainly excited in situ, but SW2 and TW3 contain significant contributions from tides propagating upward from lower altitudes. By analogy with studies for Earth's thermosphere, the DW1 amplitudes and phases are thought to reflect the combined influences of thermal expansion and vertical winds. Points of agreement and disagreement with DW1, SW2, and TW3 amplitudes and phases derived from the Mars Climate Database are noted and interpreted.

Key Points:

- Global-scale solar-synchronous tides are derived from Mars Atmosphere and Volatile Evolution Mission/Neutral Gas and Ion Mass Spectrometer measurements of CO_2, Ar, and N_2 at Mars, 150–200 km
- The diurnal tide originates mainly in situ; semidiurnal and terdiurnal tides show evidence of upward propagation from below
- Points of agreement and disagreement with the Mars Climate Database are noted and interpreted

Supporting Information:

Supporting Information may be found in the online version of this article.

Correspondence to:

J. M. Forbes,
forbes@colorado.edu

Citation:

Forbes, J. M., Zhang, X., Fang, X., Benna, M., González-Galindo, F., Forget, F., & Millour, E. (2023). Solar-synchronous tides in Mars thermosphere CO_2, Ar, and N_2 densities from MAVEN. *Journal of Geophysical Research: Space Physics*, *128*, e2023JA031637. https://doi.org/10.1029/2023JA031637

Received 24 APR 2023
Accepted 17 JUL 2023

1. Introduction

In the thermospheres of Mars and Earth, one of the most fundamental processes is the cyclic absorption of extreme ultraviolet (EUV) solar radiation due to rotation of the planet, and the resulting responses in terms of temperatures, winds and densities. Since Mars and Earth share similar rotation rates and axial tilts with respect to their orbital planes around the Sun, the responses of their upper atmospheres to this periodic forcing should share much in common. However, the relatively eccentric orbit of Mars compared to Earth ($e = 0.093$ vs. $e = 0.017$) adds an annual modulation to the seasonal variation due to axial tilt. Furthermore, at Earth, collisions of neutrals with ions constrained to global magnetic field lines ("ion drag") modify the wind field, and in turn the temperature and density response to heating by solar EUV absorption.

Empirical models of Earth's upper atmosphere, including its diurnal variation, have been formulated by fitting combined ground-based and space-based measurements from a variety of instruments and missions, spanning multiple decades and within a global framework. No such extensively observation-based model yet exists for Mars. In work leading up to the present paper, we have investigated the possibility that the Mars Atmosphere and Volatile Evolution Mission (MAVEN) has accumulated measurements of CO_2, N_2, and Ar densities between 150 and 200 km during 2015–2022 with sufficient coverage in latitude (θ), local solar time (LST) and solar longitude (Ls) such that a first glimpse of the LST variations of these densities can be delineated as a function of θ, Ls and height. It is the purpose of this paper to present some first results from this investigation.

To set the present study into a wider context, it is noted that solar radiation absorption by a rotating planet introduces periodic dependencies on both time and longitude, such that the diurnal variation of any atmospheric variable can be written as (e.g., Forbes et al., 2020):

$$\sum_s \sum_n A_{n,s}(z,\theta)\left[\cos(n\Omega t + s\lambda - \phi_{n,s}(z,\theta))\right] \quad (1)$$

where t = universal time (UT), $\Omega = 2\pi \text{sol}^{-1}$, z = altitude, λ is longitude, integer s is the zonal wavenumber, integer n defines the frequency, $A_{n,s}(z, \theta)$ is the amplitude, and $\phi_{n,s}(z, \theta)$ is the phase (i.e., longitude of maximum at 0000 UT, or UT of maximum at $\lambda = 0$). In Mars atmosphere, solar radiation is absorbed by dust, water clouds and CO_2 in the lower atmosphere (Forget et al., 1999), and by CO_2, O and a number of minor species in the thermosphere (González-Galindo, Forget, Lápez-Valverde, Angelats i Coll, & Millour, 2009).

Equation 1 represents a spectrum of "solar thermal tides" with various s and n. A zonal phase speed can be associated with each member or "component" of the spectrum: $C_{ph} = \frac{-n\Omega}{s}$, wherein $s < 0$ for eastward-propagating tides ($C_{ph} > 0$), $s > 0$ for westward-propagating ($C_{ph} < 0$) tides, and $s = 0$ for "zonally-symmetric" tides that do not propagate zonally. Moreover, if $s = n$ then $C_{ph} = -\Omega$, indicating that such tides are solar-synchronous. Historically, they are said to "migrate" westward with the apparent phase speed of the Sun to a ground-based observer, and are often referred to as migrating tides. Tides with $s \neq n$ are solar asynchronous or "non-migrating," and it is these tides that capture the longitudinal dependence of the tidal response (or source), which is primarily attributable to the influences of topography (Moudden & Forbes, 2008). Furthermore, expressing Equation 1 in terms of LST (i.e., $t_{LST} = t + \lambda/\Omega$):

$$\sum_s \sum_n A_{n,s}(z, \theta)\left[\cos(n\Omega t_{LST} + (s - n)\lambda - \phi_{n,s}(z, \theta))\right], \tag{2}$$

it is easily seen that solar-synchronous tides ($s = n$) are independent of longitude. The westward-propagating diurnal ($n = 1$, $s = 1$) and semidiurnal ($n = 2$, $s = 2$) solar-synchronous tides, denoted DW1 and SW2, respectively, are generally the largest tides forced and observed at their respective frequencies at both Mars and Earth, while the terdiurnal tide (TW3; $n = 3$, $s = 3$) is generally of secondary importance. This paper presents determinations of solar-synchronous tidal variations in CO_2, N_2, and Ar based on measurements by the Neutral Gas and Ion Mass Spectrometer (NGIMS; Benna et al., 2015; Mahaffy et al., 2015) on NASA's MAVEN (Jakosky et al., 2015; https://atmos.nmsu.edu/PDS/data/PDS4/MAVEN/ngims_bundle/).

2. Data and Methodology

2.1. NGIMS Measurements From MAVEN

MAVEN was initially placed into a 75°-inclination ~6,200 km × ~150 km elliptical science mapping orbit around Mars during late 2014. Between February 11 through 5 April 2019, an aerobraking maneuver lowered apoapsis to 4,570 km, resulting in 6.6 mapping orbits per day compared to the previous 5.3 orbits per day. For this work we use level-2, version-8, revision-1 NGIMS data with the following quality flags: IV (an abbreviation for "inbound and verified") for CO_2, IV, and OV ("outbound and verified") for N_2, and IV, IU ("inbound and unverified") and OU ("outbound and unverified") for Ar. OU data for CO_2 are excluded due to uncertainties connected with adsorption of CO_2 to the inner surfaces of the instrument (Fu et al., 2020), which is minor for the inert species N_2 and Ar. O was not included as part of this study due to similar evidence regarding instrument adsorption, and uncertainties as to whether its reactivity in Mars thermosphere would affect its interpretation in terms of tidal dynamics relative to the inert species. NGIMS collects data below 500 km altitude with most measurements exhibiting high signal to background ratio below 250 km.

Figure 1 illustrates the (a) latitude, (b) LST and (c) Ls of IV (blue) and OV (red) N_2 measurements at 180 ± 2.5 km altitude versus Earth year. In panel (d) the F10.7 solar flux measured at Earth and adjusted to Mars (MF10.7) is also plotted. Various aspects of Figure 1 will be referred to in the following.

2.2. Data Processing

In this subsection, we describe a number of data processing steps that precede organizing the data in such a way that tides can be extracted. The first step follows the traditional method of analyzing Mars data for longitude structures and subsequent examination in terms of tides (e.g., England et al., 2016, 2019; Fang et al., 2021; Liu et al., 2017; Withers et al., 2003); that is, least-squares (LSQ) fitting in longitude with respect to $k = |s - n|$ in Equation 2 where $t_{LT} \approx$ a constant. The functional form that is fit within a given interval of time is:

$$a_0 + \sum_k [a_k \cos k\lambda + b_k \sin k\lambda] \tag{3}$$

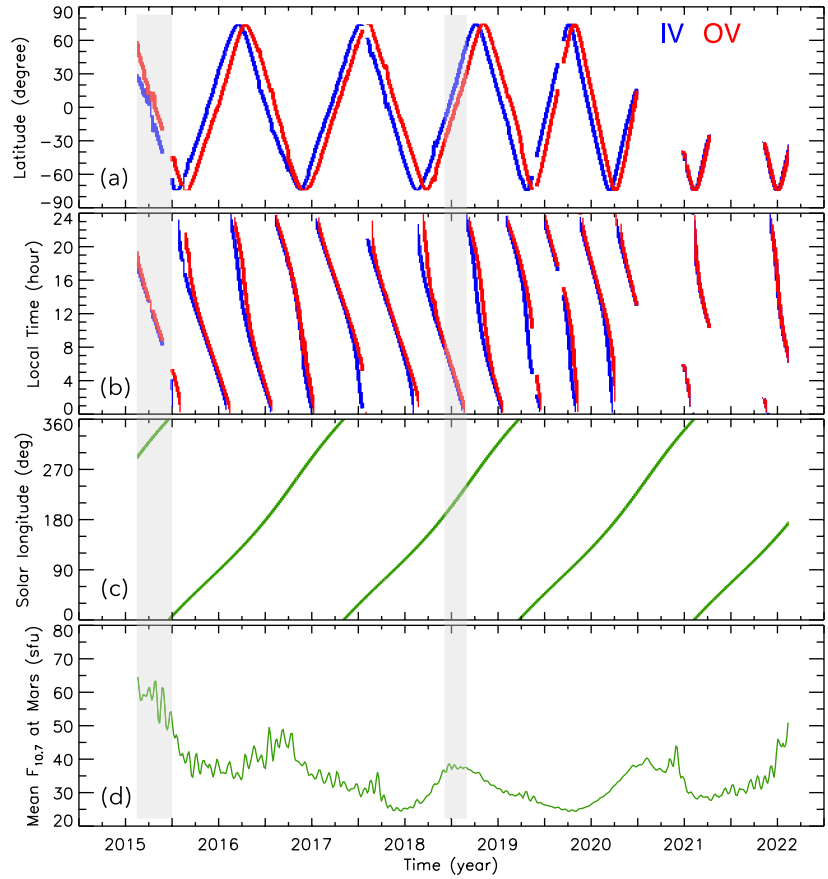

Figure 1. (a–c) Neutral Gas and Ion Mass Spectrometer sampling of Mars thermosphere versus year at 180 km, and (d) 10.7-cm solar flux (s.f.u.) corrected for Mars orbit (MF10.7). (a) Inbound (blue) and outbound (red) latitude; (b) inbound (blue) and outbound (red) local time; and (c) solar longitude, Ls. The grey shading indicates periods when data are omitted from the tidal extractions for reasons indicated in the text.

In this regard, we follow the methodology of Fang et al. (2021), except instead of focusing on a few dispersed intervals of time, we perform the fitting within sequential moving windows of fixed lengths of time throughout the time period of February 2015–February 2022. (Data during the 2018 dust storm (Ls = 190–240, MY = 34) are excluded; Guzewich et al., 2020.) As shown in Figure 1, θ, LST, Ls, and F10.7 solar flux received at Mars (MF10.7) change continuously during the acquisition of data. In addition, as Mars rotates beneath the MAVEN orbit, roughly 5 to 7 longitudes per day are sampled. Again, following Fang et al. (2021), to optimize the quality of the fits, density data are sorted into 30° longitude bins; it is required that all bins contain data; and in order to remove outliers, only data between the 10th and 90th percentiles inside each bin are used for averaging. Fits are limited to $k = 0$–3, consistent with the longitude resolution. Outlier fits with low correlation coefficients ($r < 0.6$) were also rejected based on visual examination of correlation coefficient histograms. The a_k, b_k obtained by fitting (Equation 3) were converted to amplitudes ($\sqrt{a_k^2 + b_k^2}$) and phases (longitude of maximum) and were then binned in altitude in increments of 5 km, that is, 150 ± 2.5 km to 200 ± 2.5 km. To enable characterization of our results as representative of "low solar activity" conditions, and to minimize uncertainties connected with the solar correction to be described below, a relatively small amount of data for MF10.7 > 50 during the first half of 2015 were excluded from analysis.

At a given altitude between 150 and 200 km, NGIMS made measurements as θ, LST, and Ls changed with time (see Figure 1). The choice of window length represents a balance between accumulating sufficient data to define the longitudinal structure (including the longitude- or zonal-mean, a_0), while at the same time minimizing the latitude span, which determines the latitude resolution of our final results. In order to meet the binning requirements described above and thus define a_0 and the longitudinal structure over limited ranges of LST, θ and Ls, a

window length of 15 Earth days moved forward every 5 days was chosen. Equatorward of $\theta = \pm 60°$, each of these windows spanned an average of roughly 2 hr LST, 14° latitude and 10° Ls. Between 60 and 72°S and between 60 and 72°N, LST can change much more rapidly within a 15-day window, and for the present study these regions are excluded from analysis.

Application of the above binning and fitting procedure results in a multi-year data set that consists of a_k, $k = 0$, 1, 2, 3 coefficients corresponding to CO_2, N_2, and Ar densities in Mars thermosphere, each tagged with an altitude, LST, θ, and Ls corresponding to the center of the fitting window. The ultimate goal is to depict tidal amplitudes and phases in height versus θ (hereafter htvslat) depictions at a given Ls, or θ versus Ls depictions at a given height. This requires that for every combination of θ and Ls at a given height, that sufficient LST coverage is required to extract tides. As a first step, the a_0 coefficients for all years (with the exception of the 2018 dust storm and MF10.7 > 50 as noted above) were binned with respect to Ls, θ and LST. The main constraint was to define $\theta \times$ Ls bins large enough that they contained sufficient LST coverage, yet small enough that physically meaningful depictions of the θ and Ls dependences of tides could be constructed. After some trial and error with various-sized bins in Ls (i.e., 360, 180, 120, 90, 60), θ (24°, 12°), and LST (1, 2, and 4 hr), we arrived at 120°-Ls bins slipped every 30° Ls, and latitude bins 24° wide slipped every 12°, and 2 hr LST bins. (See Section 2.3 for a validation of this choice.) Note that the most poleward 24° bins (i.e., centered on 48°S and 48°N) include data from 36° to 60°S and 36°–60°N, and thus include data up to 60°S and 60°N. Average values of a_0 were calculated within each bin along with the associated standard deviation. For the remainder of this paper, the focus is on sun-synchronous tides, and hence on analysis of the a_0 values. The remaining wave components are set aside for future analyses.

As a result of the above binning, not all bins were populated. A two-step interpolation procedure was followed to fill in the gaps, as follows. The starting points are the 120 latvsLs arrays of a_0 values for each 2 hr LST bin (designated "latvsLs$_0$"), and the 120 latvsLST arrays of a_0 values for each 120°-Ls bin (designated "latvsLST$_0$"), obtained from binning and averaging as described above. In the first step, the latvsLs$_0$ arrays were interpolated based on 2-D nearest-neighbor linear interpolation, leading not only to new latvsLs arrays designated "latvsLs$_1$," but also to new latvsLST arrays designated "latvsLST$_1$." These latvsLST$_1$ arrays were similarly interpolated, leading to the final fully-populated latvsLST$_2$ and latvsLs$_2$ arrays. No further iterations were necessary to populate all bins.

The total number of a_0 values were about the same for Ar and N_2, namely about 360 at 150 km, 540 at 155 km, and 665–885 at any given height from 160 to 200 km. The number of CO_2 a_0 values available for analysis were about half these numbers. Furthermore, the percentages of latvsLST bins populated for any given Ls, or latvsLs bins populated for any given LST, prior to interpolation were on average $\gtrsim$85% for Ar and N_2 without much dependence on altitude. The corresponding percentages of populated bins for CO_2 were usually <70% with some two-dimensional gaps in the latvsLST and latvsLs arrays that were judged to be too large to produce results at a similar level of confidence as those based on Ar or N_2. We take the conservative approach here and confine the majority of the following results to Ar and N_2. However, we begin the following Results section with a couple of cases wherein data coverage for IV CO_2 permits comparison of tidal perturbations in CO_2, Ar, and N_2 densities. And, despite the fewer numbers of points at 150 and 155 km, in most cases the htvslat depictions to be presented in Section 3 show reasonable continuity with higher altitudes, and therefore the tidal information presented there cover the full 150–200 km range of altitudes.

The robustness of the results at 150–160 km noted above also supports our contention that delineation of thermosphere tides at Mars based on multi-year sampling is a reasonable thing to do, and is scientifically informative. This is frequently and successfully done for the tidal spectrum propagating vertically into Earth's thermosphere (e.g., Oberheide et al., 2011; Truskowski et al., 2014), as well as tides excited in situ in the thermosphere by solar radiation absorption (Emmert et al., 2020). At Mars, it is unlikely that DW1 originating in the lower atmosphere will penetrate significantly above 150 km (Forbes et al., 2020), but SW2 can penetrate well above 150 km. Based on MCS data, the tides emanating from the middle atmosphere show a high degree of repeatability from year to year (e.g., Moudden & Forbes, 2015; Wu et al., 2015). Furthermore, at Mars there is no documented evidence of any significant competition from variability of solar wind origin below 200 km, and no significant driving of the neutral atmosphere by a variable ionosphere.

There is one source of variability of potential relevance, and that is due to the EUV solar flux that is absorbed in Mar's thermosphere, and that gives rise to solar-synchronous tides generated in situ. At Mars, this consists of a component due to the quasi-27-day rotation of the Sun (Forbes et al., 2008; Hughes et al., 2022), usually prevalent during solar maximum, a long-term ("solar cycle") component (Fang et al., 2022; Forbes et al., 2008), and an

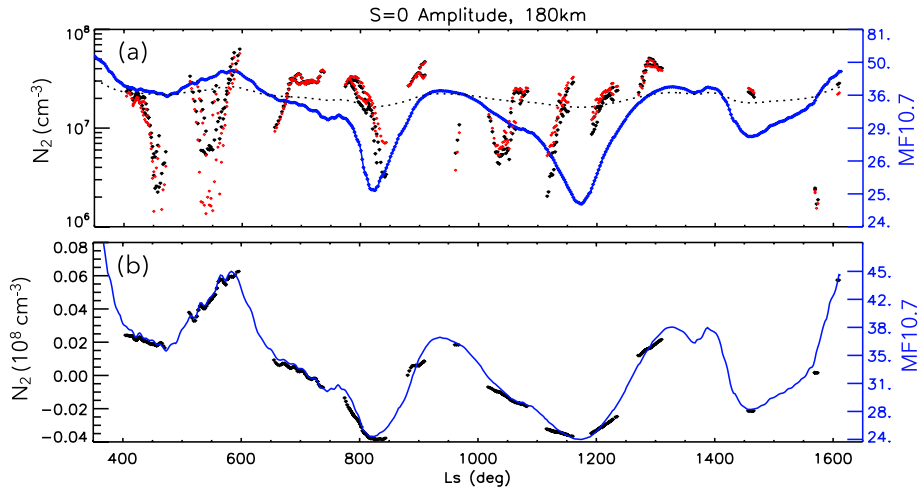

Figure 2. (a) Amplitude a_0 of N_2 density (black and red dots) at 180 km, and 40-Ls mean of MF10.7 (blue line), versus Ls covering the same period of time as in Figure 1. The black dots represent N_2 densities assigned to latitudes between 48°S and 48°N, which reflect a combination of latitude, Ls and LST variations. The black dotted curve represents the least squares fit of the MF10.7 curve to these N_2 densities, which consists of a mean term and a linear term proportional to MF10.7, which represents the MF10.7 variability in N_2. The red dots represent the black dots with the MF10.7 variability removed. (b) The removed latitude-independent MF10.7 variability in N_2 a_0 and MF10.7 are re-plotted with a *y*-axis scale that better visualizes the long-term trend and the orbital effect.

annual variation due to the eccentricity of Mars orbit around the Sun combined with the $1/R^2$ dependence of solar flux where R is the distance from the Sun (Fang et al., 2022; Forbes et al., 2008). All of these are clearly evident in the MF10.7 plot in Figure 1. Therefore, an MF10.7 correction was devised and applied to the a_0 amplitudes analyzed here, as explained in the following two paragraphs.

The a_0 amplitudes at a given θ and height represent zonal means at a specific LST and MF10.7. Our approach is to gather all a_0's from various years throughout the MAVEN mission, and organize them into 2-hr LST bins within a given $\theta \times$ Ls $\times$ 5-km height bin prior to decomposition into DW1, SW2, and TW3 tidal components through LSQ fitting. That LSQ fitting also establishes the diurnal- and zonal-mean (DZM) background that serves as a reference for the DW1, SW2, and TW3 perturbations. However, binning with respect to Ls and LST involves combining data from different levels of MF10.7. Since each a_0 value contains a part that is connected with a background that is MF10.7-dependent, and a part that represents the LST-dependent perturbation with respect to that background, the two parts must be separated before decomposing the LST-dependent part into tidal components. Otherwise, the MF10.7 variability in the background can alias into the LST variation and thereby influence extraction of DW1, SW2 and TW3.

The following steps were taken to remove solar flux variations from the a_0 data series prior to binning. Refer to the example in Figure 2 for N_2 at 180 km. The blue curve in Figure 2a represents the 40-Ls running mean of MF10.7, and contains signatures of a long-term trend and the orbital effect, the latter being dominant given the MF10.7 < 50 restriction. The black dots represent N_2 densities assigned to latitudes between 48°S and 48°N, which reflect a combination of θ, Ls and LST variations. The dotted curve represents the LSQ fit of the MF10.7 curve to these N_2 densities, which consists of a mean term and a linear term proportional to MF10.7, which represents the MF10.7 variability in N_2. The red dots represent the black dots with the MF10.7 variability removed. The removed MF10.7 variability is replotted in Figure 2b with a *y*-axis scale that better visualizes the trend and the orbital effect. The inclusion of all data between 48°S and 48°N results in an average MF10.7 correction across these latitudes, a compromise necessitated by the sparsity of data. Comparisons between tidal depictions obtained with and without MF10.7 variability removed are shown later in this paper to demonstrate the impacts of this correction, which turn out to be modest.

2.3. Mars Climate Database (MCD)

The MCD (http://www-mars.lmd.jussieu.fr) provides meteorological fields based on the Mars Planetary Climate Model (Mars PCM) formerly known as the LMD Mars GCM (General Circulation Model) which has its roots

in the work of Forget et al. (1999), but which has been further developed to extended into the thermosphere and ionosphere (González-Galindo et al., 2013, 2015; González-Galindo, Forget, Lápez-Valverde, Angelats i Coll, & Millour, 2009), and to include improved treatments of dust and water cycles, photochemistry, radiative transfer, and solar radiative fluxes. In this paper, we employ the MCD for the dual purpose of assisting in the analysis and interpretation of the MAVEN tidal results, and for assessing the ability of the MCD to characterize sun-synchronous tides in Mars thermosphere. Herein we use the "climatology" scenario from MCD Version 5.3 (Millour et al., 2018), in which dust distributions are based on those observed in Mars years when no global dust storms occurred, minimum solar EUV conditions are assumed, and model outputs are available every 30° Ls.

A check was performed on the viability of the 24° latitude bins slipped every 12°, and 120°-Ls bins slipped every 30° to meaningfully characterize the θ and Ls structures of tides. This was done by extracting tides from the MCD based on its 3° latitude and 30° Ls resolutions, and then comparing with those tides extracted based on the MAVEN binning. The results compared favorably at a sufficiently high degree of fidelity to support the choices made for the MAVEN analysis. Some typical examples are provided in Figure S1 of Supporting Information S1. The totality of these results leads us to conclude that the results to be presented in the next section represent realistic depictions of actual tides in Mars thermosphere, albeit somewhat smoothed in θ and Ls.

3. Results

3.1. Results for CO_2, Ar, and N_2

As noted previously, given the reduced number of data points for CO_2 compared to Ar and N_2, there is limited opportunity to compare tidal variations obtained from contemporaneous measurements of all three constituents. However, one example where the coverages of CO_2, Ar, and N_2 were compatible is illustrated in Figure 3 in the form of latvsLST plots for the Ls = 90° ± 60° bin at 180 km. Boxcar smoothing was used to clean up noise in the MAVEN depiction and to optimize comparisons with the model without much loss in amplitude of the salient features. The diurnal cycles of CO_2, Ar, and N_2 are of order ±30%–65%, ±30%–70%, and ±30%–55% about the DZM for MAVEN (top row), and ±30%–60%, ±35%–45%, and ±12%–25% for MCD (second row). There is also a clear difference in the LST of maxima between MAVEN and MCD, with maxima for MAVEN occurring between 12 and 18 hr, as compared with 10–14 hr (CO_2 and Ar) and 8–12 hr (N_2) for MCD.

The uncertainties in the a_0 amplitudes displayed in Figure 3 are related to the standard deviations σ of the a_0 amplitudes obtained within each 15-day fit to the longitudinal structures described previously. The median (mean) values of these σ are 6.5% (8.4%) for CO_2, 5.1% (6.5%) for Ar, and 4.7% (6.2%) for N_2. The likely dominant contributor is geophysical, originating from day-to-day and longitudinal variability associated with non-steady tides, gravity waves (GWs) and planetary waves. Since the number of points within any given LST bin is often less than 10, the sample sizes are too small compared to the total population to apply a $1/\sqrt{(N)}$ reduction in these values based on random sampling. However it does seem reasonable to state that these σ represent a reasonable approximation of the uncertainties associated with the a_0 amplitudes in Figure 3.

The top two rows in Figure 3 were decomposed into DW1, SW2, and TW3 components through LSQ fitting of the following functional form at each latitude:

$$\sum_{n=1}^{n=3}(a_n \cos n\Omega t_{LT} + b_n \sin n\Omega t_{LT}) \tag{4}$$

This fitting yields amplitudes $\left(\sqrt{a_n^2 + b_n^2}\right)$ and phases (LST of maximum, $\frac{1}{n\Omega}\arctan\left(\frac{b_n}{a_n}\right)$) of DW1 ($n = 1$), SW2 ($n = 2$) and TW3 ($n = 3$). Each of these components was then reconstructed as a function of θ and LST and examined separately. DW1 is illustrated in the bottom two rows of Figure 3 for MAVEN and MCD, and a comparison between MAVEN and MCD for SW2 is provided in Figure S2 of Supporting Information S1 for the interested reader. In this particular case, that is, Ls = 90 at 180 km, it is evident by comparison with the top two rows of Figure 3 that the diurnal variation is dominated by DW1 for both MAVEN and MCD for all 3 constituents, although a semidiurnal contribution is clearly visible for MCD in the Southern Hemisphere (SH) (i.e., note the secondary maxima at LST = 22 hr). The semidiurnal and terdiurnal variations were $\lesssim$±17% (36%) and ±9% (9%) for MAVEN (MCD), and are not considered further at this point. For DW1, the noteworthy differences between MAVEN and MCD are similar to those expressed above for the total diurnal variation: For MAVEN, the DW1

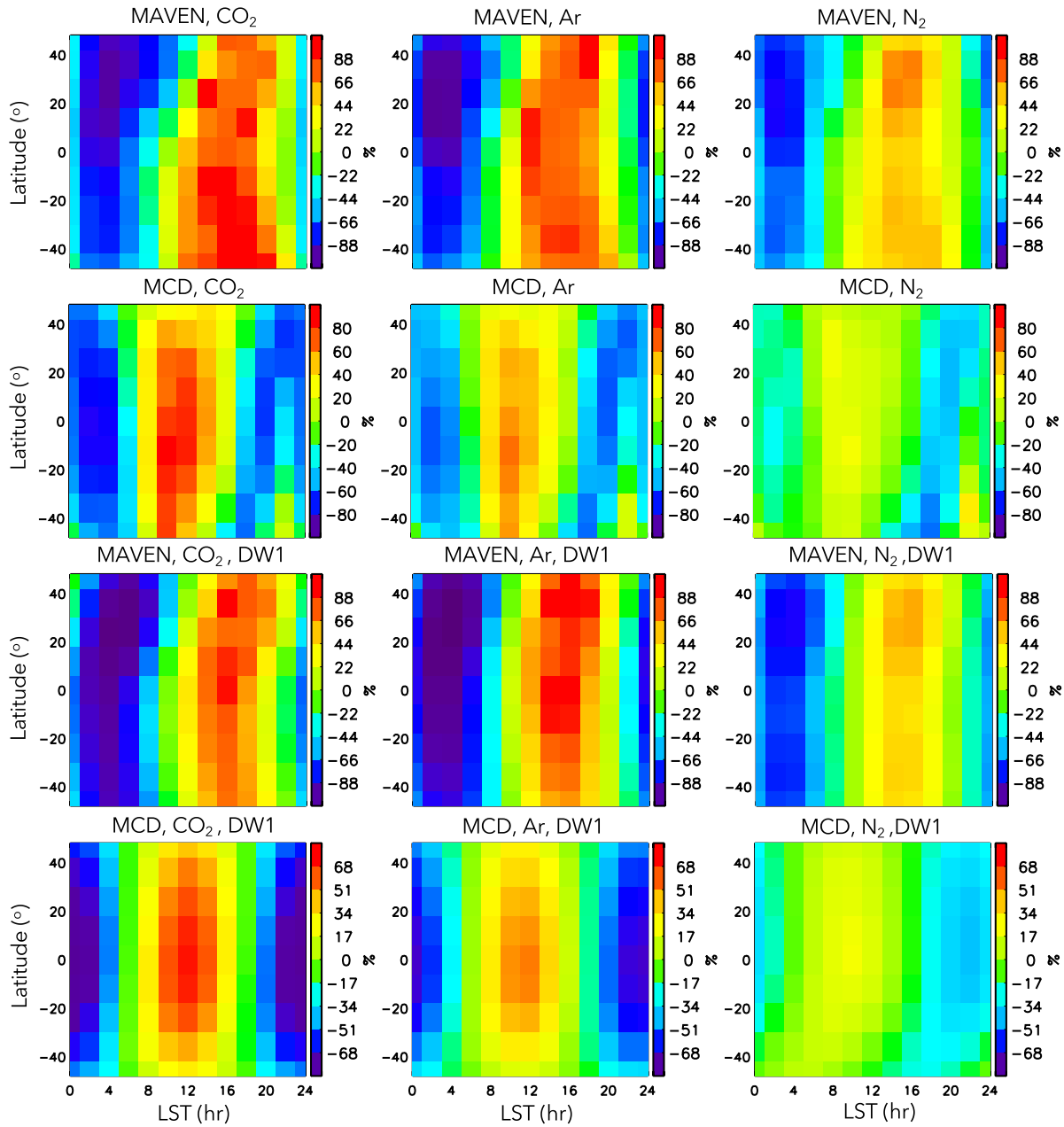

Figure 3. LST variation of CO_2, Ar, and N_2 (left to right) densities (expressed in % with respect to their DZM values) between ±48° latitude for Ls = 90 ± 60 at 180 km. Top row: Mars Atmosphere and Volatile Evolution Mission (MAVEN). Second row: Mars Climate Database (MCD). Third row: diurnal component (DW1) of MAVEN data in top row. Bottom row: diurnal component (DW1) of MCD data in second row. SW2 results are shown in Figure S2 of Supporting Information S1.

amplitudes range between 70% and 90% for CO_2 and Ar and 30%–45% for N_2, whereas for MCD the values are 30%–70%, 20%–40% and ~20% for N_2. And, the phases for MAVEN DW1 are roughly 2–4 hr later than MCD for CO_2 and Ar, and 4–6 hr later for N_2. Given the ~5%–6% σ quoted above relative to the MAVEN amplitudes depicted in Figure 3, it is concluded that these differences between observations and modeling are real.

Given that the molecular weights of CO_2, Ar, and N_2 are 44, 40, and 28, respectively, the corresponding decreases in the DW1 density responses in Figure 3 suggest a connection. This dependence on molecular weight is also reminiscent of results obtained by England et al. (2016) in their analysis of NGIMS data. They noted a scale height dependence of maxima-minima differences in longitudinal fits of the type expressed in Equation 3 to CO_2, Ar, N_2, O and He densities. England et al. (2016) furthermore interpreted their results using an analytic formula

derived by Dudis and Reber (1976) for thermosphere GWs, who validated their theoretical predictions against GWs observed in Atmosphere Explorer-C mass spectrometer measurements at Earth.

Dudis and Reber's (1976) approach involved using the linearized GW equations to derive and manipulate formulas that relate GW constituent density fluctuations to GW vertical velocities under the assumption that the time scale for wave oscillations is much shorter than the diffusion times for individual constituents; in other words, any diffusive separation resulting from the wave motion itself is neglected. In their application, this required that the wave periods needed to be sufficiently short: at an altitude of 200 km, periods $\lesssim$45 min for a wave with 400 km horizontal wavelength. Based on diffusion coefficients and relationships in Nair et al. (1994) and Nair (1996), a nominal density of 2×10^8 cm^{-3} for N_2 at 180 km, a nominal scale height (H) of 25 km for N_2, the time constant for N_2-CO_2 diffusion at 180 km in Mars thermosphere is calculated to be $\tau = H^2/D = 21$ min where D is the N_2-CO_2 diffusion coefficient $= 0.5 \times 10^{10}$ cm^2 s^{-1}. Therefore, in Mars thermosphere the wave periods would have to be significantly shorter than 21 min for Dudis and Reber's (1976) criterion to apply. These values are clearly out of the range of those applicable to the solar-synchronous tides considered in this paper. Nevertheless, it is instructive to apply their equation to the problem at hand to demonstrate its inapplicability, and to provide context for discussions and interpretations in Section 3.3.

Equation 12 of Dudis and Reber (1976) relates the GW-induced perturbation density for an individual constituent (ρ_c') relative to its mean ($\bar{\rho}_c$) to the GW-induced perturbation of the average density (ρ') and its mean value ($\bar{\rho}$) in terms of the mean molecular weight (M), the molecular weight of an individual constituent (M_c), and the ratio of specific heats (γ):

$$\frac{\rho_c'}{\bar{\rho}_c} = \frac{\gamma M_c - M}{(\gamma - 1)M} \frac{\rho'}{\bar{\rho}} \tag{5}$$

At 180 km at Mars, CO_2 is the dominant constituent (Mahaffy et al., 2015), so $M = 44$, and $\gamma = 1.3$; and $M_c = 40$ for Ar and $M_c = 28$ for N_2. According to the above expression upon insertion of these numbers, and based on a 70% $\rho'/\bar{\rho}$ perturbation for CO_2, the MAVEN Ar(N_2) density perturbations ought to be 42% (−40%), the negative value implying an out-of-phase relationship. For MAVEN, the Ar(N_2) expected density perturbations are 48% (−46%) based on an 80% perturbation for CO_2. These predictions are clearly not in accord with those depicted in Figure 3. As noted in Section 4, applicable modeling results for Earth's thermosphere indicate that there are other processes to be considered in the case of tides versus GWs in the thermosphere.

There is an additional opportunity wherein coverage is sufficient to compare CO_2, Ar, and N_2 tidal responses, and this is in connection with the annual mean. In fact, for the annual mean, it is possible to capture the height dependence of the tides across the full 48°S–48°N range of latitudes. For thermosphere tides excited by in situ absorption of solar radiation, it can be argued that an annual-mean depiction of solar tides is physically meaningful, since the forcing is persistent throughout the year, just slowly migrating from hemisphere to hemisphere in accord with the sub-solar point. The tradeoff obtained by averaging over seasons is the ability to see the height versus θ (htvslat) distributions of DW1, SW2, and TW3 for all three constituents. At least for Ar and/or N_2, annual-mean tides can also be placed into context by viewing the Ls variability of these tides, which is done in Section 3.2.

Such htvslat depictions are provided in Figure 4. The top two rows compare DW1 density perturbations between MAVEN (top row) and MCD (second row) for CO_2, Ar, and N_2 (left to right), and the bottom two rows similarly compare SW2 density perturbations. The similarity of Ar and CO_2 density perturbations in Figure 4 suggests that Ar can be used as a reasonable proxy for CO_2 insofar as solar-synchronous tides are concerned for both MAVEN and MCD. Moreover, N_2 density variability exhibits sufficient departures from CO_2 and Ar behaviors to suggest that N_2 abides by somewhat different physics, presumably due to its smaller molecular weight.

Similar to the results for Ls = 90 and 180 km in Figure 3, the annual-mean DW1 in Figure 4 for CO_2 and Ar are about 40% smaller for MCD than MAVEN, and this difference is even larger for N_2. Moreover, a major structural difference now exists between N_2-DW1 in MAVEN and in MCD. Whereas N_2-DW1 is similar in structure to CO_2-DW1 and Ar-DW1 in both MAVEN and MCD, N_2-DW1 in the MCD exhibits maxima at 200 and 150 km. Examination of temperatures and densities in the MCD over wider height and latitude ranges reveals that the lower-altitude maximum is associated with a second response, other than that due to direct insolation absorption, peaking near 120 km and in anti phase with the response at higher altitudes. This structure is most evident between Ls = 180 and Ls = 330, and occurs to a much lesser degree for Ar (see following subsection).

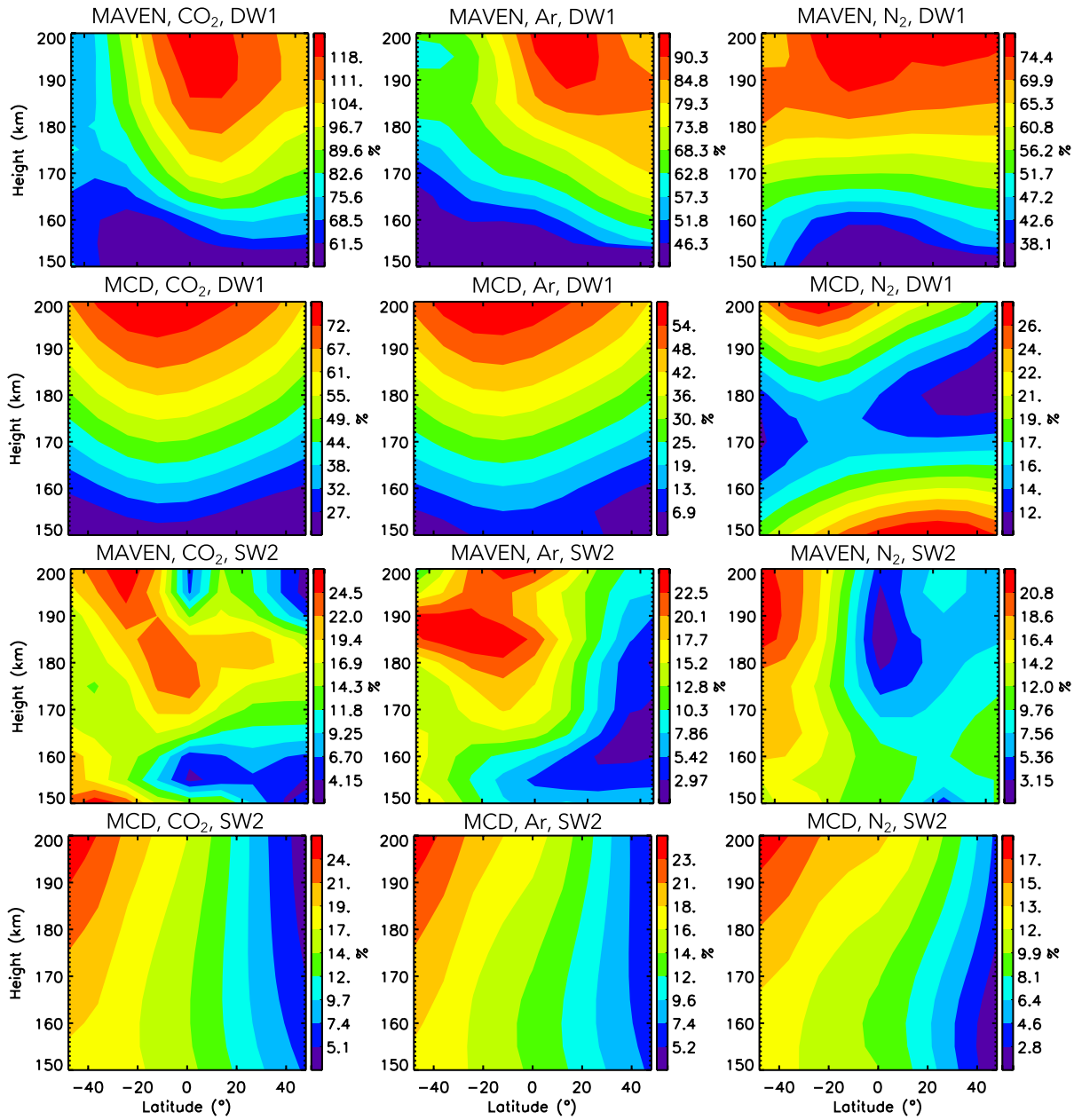

Figure 4. Htvslat depictions of annual-mean DW1 (top two rows, Mars Atmosphere and Volatile Evolution Mission (MAVEN) above Mars Climate Database (MCD)) and SW2 (bottom two rows, MAVEN above MCD) migrating tide amplitudes of CO_2, Ar, and N_2 (left to right) densities, expressed in % with respect to their DZM densities.

The comparable amplitudes originating at high and low altitudes in antiphase explains the interference pattern depicted in Figure 4 for N_2-DW1 in the MCD. Perhaps the most important point to take away from this part of the presentation is that there is no evidence of a lower-altitude response in the MAVEN data above 150 km.

The bottom two rows of Figure 4 contain similar comparisons between CO_2, Ar, and N_2 MAVEN and MCD responses for SW2. The MAVEN responses are all similar in magnitude, and share the common feature of extending from low latitudes at lower heights to higher latitudes and heights in the SH. The MCD SW2 structures similarly increase simultaneously with height and θ, but tend more to occupy both hemispheres between $\theta = \pm 48°$. This increase in MCD SW2 toward SH mid-latitudes was also noted in connection with Figure 3. The maximum MCD SW2 amplitudes are similar in magnitude to those of MAVEN, and N_2 in both MAVEN and MCD exhibit very modest decreases in amplitude with decreasing molecular weight as compared with DW1.

The above results for annual-mean solar-synchronous tides are now put into context in the following subsection, where htvslat and latvsLs structures for DW1 and SW2 for Ar and N_2 are examined.

3.2. Global-Scale Views of Tides in Ar and N_2

As noted in the Introduction, N_2 and Ar densities measured by NGIMS have superior coverage and reduced uncertainties compared with CO_2. Therefore, for the purposes of gaining a truly global perspective of migrating tides in Mars thermosphere, we restrict our attention to Ar and N_2 densities. Equation 4 was applied to MAVEN and MCD % density residuals for each height, θ and Ls bin, yielding amplitudes and phases of DW1, SW2, and TW3 every 12° latitude, 30° Ls, and 5 km altitude, from which htvslat and latvsLs plots can be constructed at fixed Ls and fixed heights, respectively. It is the purpose of this subsection to present and discuss these htvslat and latvsLs depictions. For MAVEN, LSQ fitting also yields standard deviations of amplitude and phase that are based on the residuals of the data from the fits as expressed in Equation 4. However, these σ ($\lesssim$1% for DW1, SW2, TW3 amplitudes; $\lesssim$0.04P hr where P is the wave period) are considerably smaller than those ∼5%–6% σ associated with the binned a_0 amplitudes noted previously. Therefore, it seems most credible to adopt the former values as lower limits, and the latter as a more realistic measure of uncertainty in the amplitudes; however, the σ of the phases are not quantifiable using the latter metric.

Figure 5 provides htvslat depictions of Ar-DW1 amplitudes (top two rows) for MAVEN (upper) and MCD (lower) for Ls = 90, 180, and 270 (left to right), while the bottom two rows provide the same depictions for N_2-DW1 These figures capture the essence of the DW1 variations within a MY, recalling that each of these is a ±60-Ls mean. Similar depictions of DW1 phases are provided in Figure S4 of Supporting Information S1. For Ar, MAVEN DW1 maximum amplitudes decrease from ∼120% near 195 km to ∼95% near 180 km from Ls = 90 to Ls = 270, while MAVEN DW1 maximum amplitudes for N_2 remain near ∼75% throughout the MY without a discernible downward shift in altitude of maximum, which could be masked by the 200 km altitude limit on the displayed data. For both Ar and N_2, DW1 amplitudes are noticeably more confined to upper levels for Ls = 180 and Ls = 270 as compared with Ls = 90. Examination of MAVEN phases reveals that there is evidence of downward phase progression below 170 km, somewhat greater for Ls = 270 as compared with Ls = 180, which would be consistent with vertical propagation of DW1 excited in the lower atmosphere into the region. The progressive contraction of contours to higher altitudes from Ls = 90 to Ls = 270 could be a signature of phase interference between DW1 generated in situ and that propagating from below.

Given the limitations on data sampling covering multiple years, it is unwise to comment further on other than the salient MAVEN structures in Figure 5. Of particular note is the fact that the largest MF10.7 correction occurs in the vicinity of Ls = 90, mainly apparent in SH amplitudes (see Figure S5 in Supporting Information S1). Referring to Figure 2, the larger correction near Ls = 90 has its origins in the MF10.7 orbital effect, which has its minimum around Ls = 90 in the SH for each MY. The correction is progressively less noticeable in Figure 5 from Ls = 90 to Ls = 180, and from Ls = 180 to Ls = 270, and does not affect the conclusions drawn above regarding the presence of vertically-propagating DW1.

The MCD Ar-DW1 amplitudes in Figure 5 at Ls = 90 are broadly similar to MAVEN in that they both maximize near 200 km at low latitudes and extend down to 150–160 km; however, the MCD amplitudes are about 40%–60% those of MAVEN. Proceeding from Ls = 90 to Ls = 270, there is also an increased contraction of the amplitude contours at the lower heights, but for MCD the underlying origin is different than for MAVEN. As noted previously in connection with Figure 4, there is a secondary source of DW1 at lower altitudes but it is not upward-propagating. Indeed, there is instead evidence of upward phase progression, which is the result of phase interference between the in situ source which has its maximum near noon, and a lower-thermosphere source which has its maximum near midnight. One can readily see in the bottom-row panels of Figure 5 that the change in htvslat structure from Ls = 90 to Ls = 270 is even more extreme for N_2. Further discussion of this behavior in the MCD is provided in the following subsection.

Figure 6 provides the analog of Figure 5 for SW2. Phases are provided in Figure S6 of Supporting Information S1. Beginning with Ar for MAVEN in the top row of Figure 5, the obvious differences from DW1 are the smaller amplitudes (maxima ∼15%, 25%, and 30% for Ls = 90, 180 and 270, respectively), and the much different htvslat structures. For Ls = 90 the SW2 response basically only occupies the Northern Hemisphere (NH), although a hint of the NH vertical structure at 20°N exists near 48°S. For Ls = 180 and 270, with the exception of higher-altitude

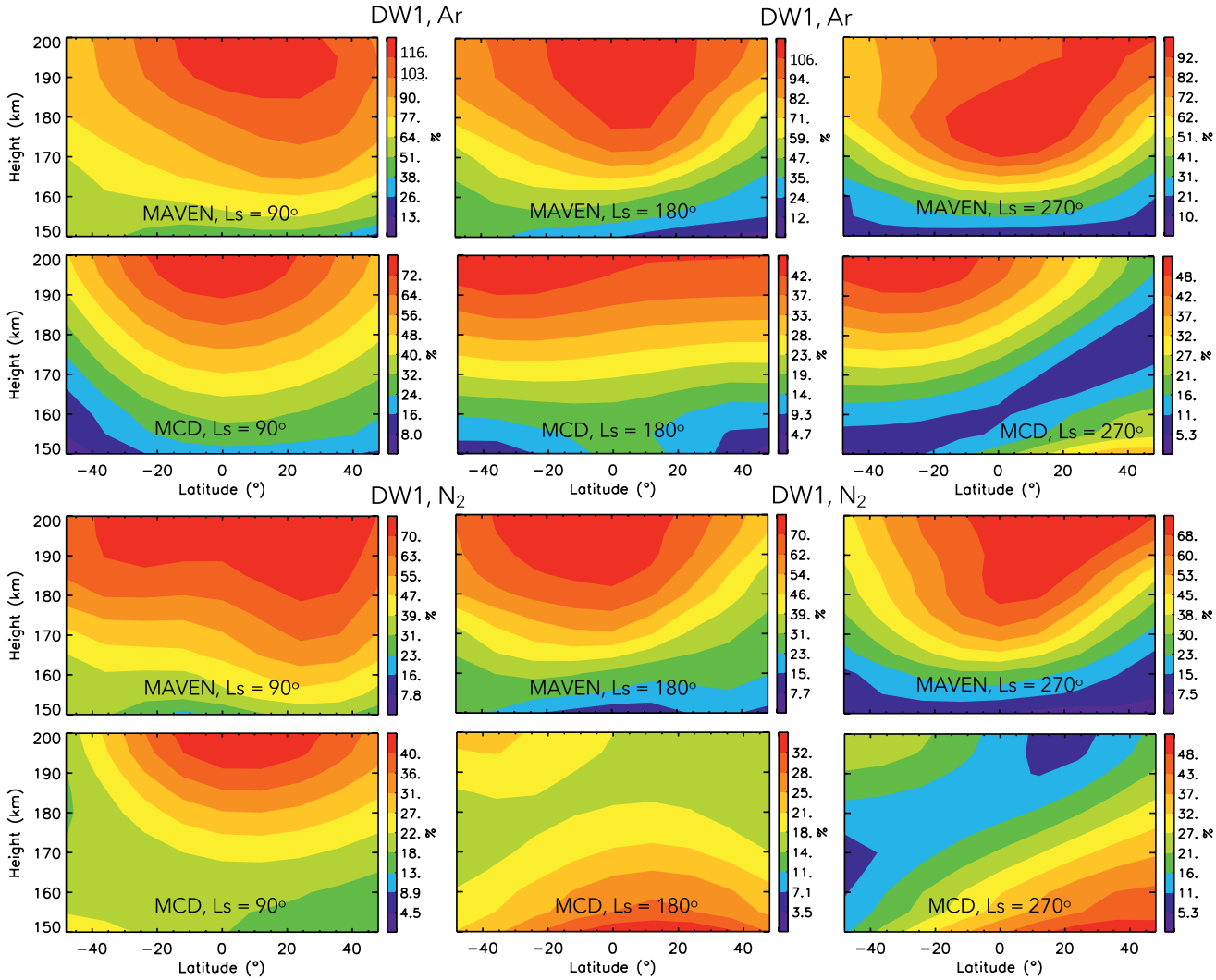

Figure 5. Htvslat depictions of DW1 amplitudes of Ar (top two rows, Mars Atmosphere and Volatile Evolution Mission (MAVEN) above Mars Climate Database (MCD)) and N_2 (bottom two rows, MAVEN above MCD) for Ls = 90 ± 60 (left), Ls = 180 ± 60 (middle), and Ls = 270 ± 60 (right). DW1 phases are shown in Figure S3 of Supporting Information S1.

signatures at middle latitudes in the SH, the SW2 htvslat structures are maximum in the 160–175 km region and are similar to those depicted in the annual mean for Ar-SW2 in Figure 4. The phases in Figure S6 of Supporting Information S1 definitively indicate upward propagation (downward phase progression), with the phase progression being more prominent and extending to higher altitudes for Ls = 180 as opposed to Ls = 270, and are not so apparent for Ls = 90. These results suggest the greater relative influence of in situ generated SW2 for Ls = 90 and Ls = 270, but the upward-propagating and in situ responses cannot be quantitatively separated. For N_2 in the third row of Figure 6, the MAVEN htvslat structures for Ls = 180 and Ls = 270 tend to be more confined to middle latitudes and higher altitudes in the SH (with their main maximum occurring there), and possess smaller amplitudes at low latitudes and altitudes than Ar; these features are consistent with the annual-mean depiction for N_2-SW2 in Figure 4, and the differences therein from Ar. For Ls = 180 and Ls = 270, the degrees of phase progression depicted in Figure S6 of Supporting Information S1 are less for N_2 than Ar.

For reference, comparisons of the MAVEN SW2 results in Figure 6 with those without the MF10.7 correction are provided in Figure S7 of Supporting Information S1. The differences are even more modest than for DW1, and do not bear any relevance to the conclusions drawn above.

The MCD SW2 results in the second and bottom rows of Figure 6 differ markedly from those of MAVEN, and phases in Figure S6 of Supporting Information S1 reflect only the slight presence of vertically propagating SW2

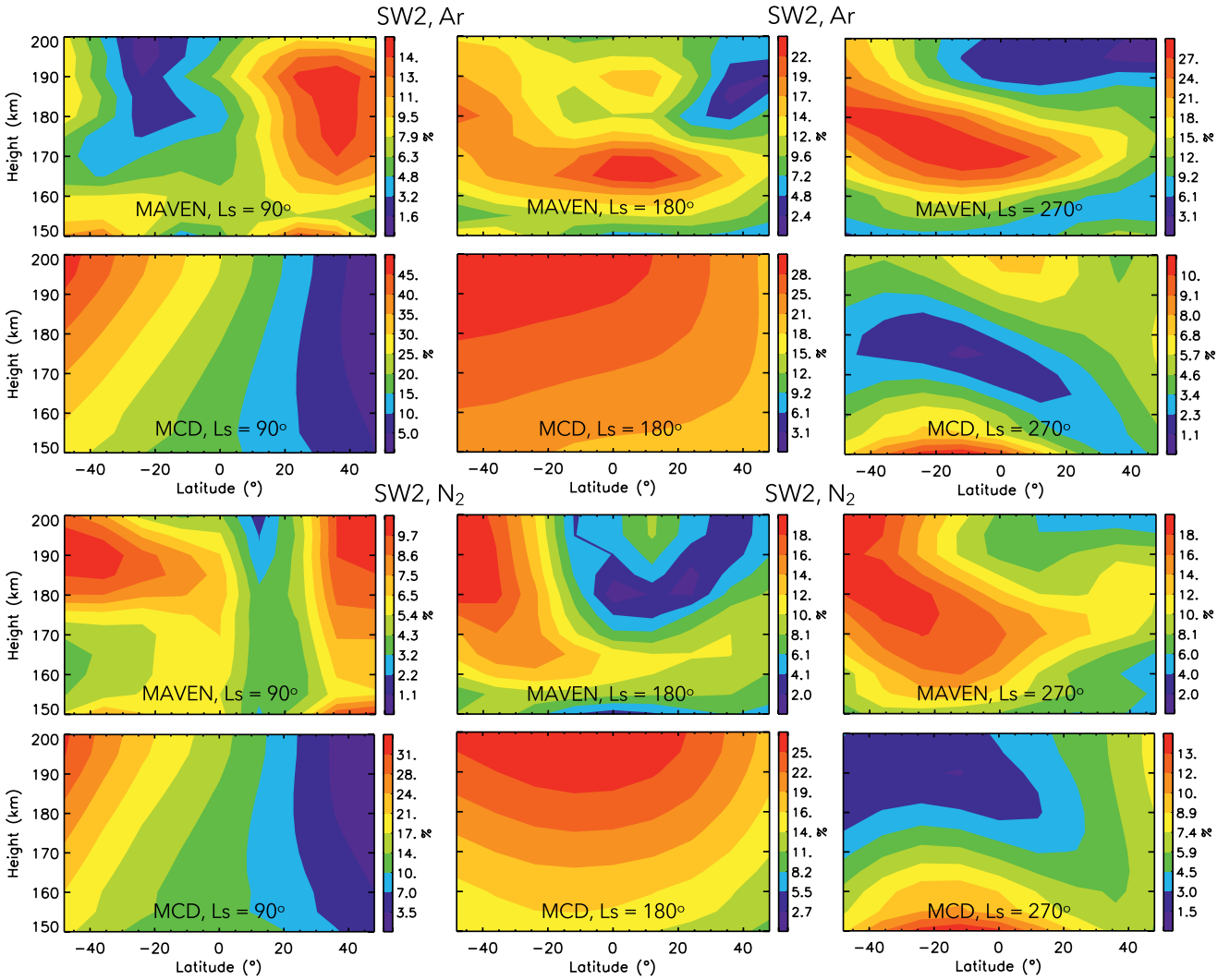

Figure 6. Same as Figure 5, except for SW2. SW2 phases are shown in Figure S5 of Supporting Information S1.

in the NH for Ls = 180 and in the SH in the vicinity of 48°S for Ls = 90. Otherwise, there is no indication of phase progression with height. For Ls = 270, an interference pattern similar in type noted for DW1 exists for SW2 in Figure 6, accompanied by upward phase progression (see Figure S6 in Supporting Information S1).

The latvsLs structures of DW1 and SW2 responses for Ar and N_2 in Figure 7 provide some insights complementary to those provided by the previous htvslat depictions. For DW1-Ar the latvsLs structures are very similar between MAVEN and MCD, but departing significantly for Ls > 180 due to the interference effects noted above for MCD. The similarity holds for DW1-N_2 at 180 km, but is absent at 160 km. A common feature of SW2 in this figure between MAVEN and MCD is the tendency for SW2 to be confined to the SH for both Ar and N_2. At 160 km, for both Ar and N_2, SW2 occurs around Ls = 30 to Ls = 180 at 48°S for MCD and Ls = 120 to Ls = 180 for MAVEN, with excursions into the NH occurring around Ls = 180 for both MAVEN and MCD.

The analogs for Figure 5 and Figure S4 in Supporting Information S1 for DW1, and Figure 6 and Figure S6 in Supporting Information S1 for SW2, are provided in Figures S8 and S9 of Supporting Information S1 for TW3. These results are not presented, or are a focus of discussion, in the main text due to their relatively small amplitudes ($\lesssim$10%) and greater relative uncertainties than DW1 and SW2. The main relevant points are (a) the htvslat structures for N_2 are very similar to those of Ar, although maximum amplitudes are 30%–50% smaller; (b) phase progression consistent with vertical propagation exists in the MAVEN htvslat structures for Ls = 90, 180 and 270, but is virtually absent in the MCD results for Ls = 90 and Ls = 180; (c) for Ls = 270, htvslat amplitudes

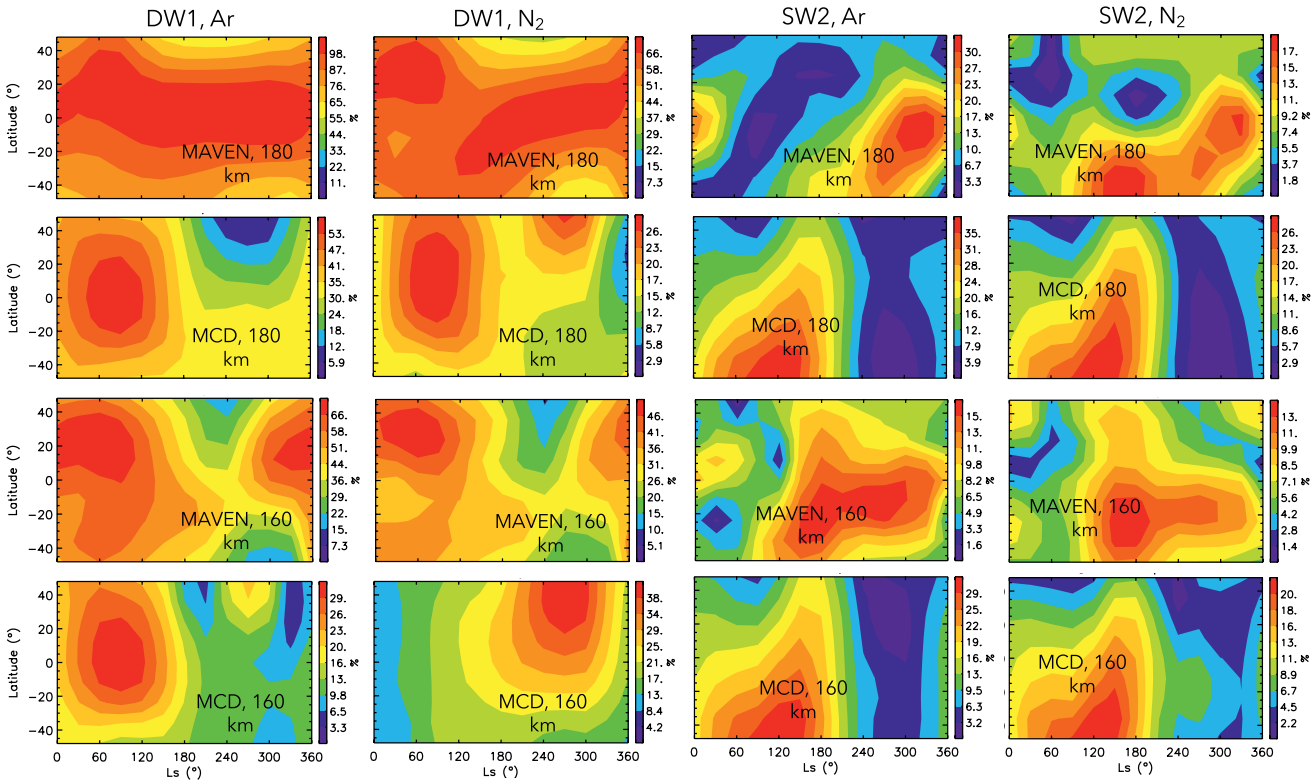

Figure 7. LatvsLs depictions of DW1 density amplitudes in % (left 2 columns, N_2 densities to right of Ar densities) and SW2 density amplitudes in % (right 2 columns, N_2 densities to right of Ar densities) at 180 km (top two rows, Mars Atmosphere and Volatile Evolution Mission (MAVEN) above Mars Climate Database (MCD)) and 160 km (bottom two rows, MAVEN above MCD).

structures suggesting interference effects similar to DW1 and SW2 are present in the MCD results, but in this case some phase progression consistent with upward propagation is present. This basic structure is repeated for MCD at 180 km, and nearly so for MAVEN N_2 at 180 km; however, the occurrence of MAVEN SW2-Ar in the SH is shifted to later in the year.

3.3. Interpretation of Results

There are no references that deal with the relative tidal responses of CO_2, Ar and N_2 in Mars thermosphere. However, there are some terrestrial works (Mayr & Harris, 1977; see also Forbes, 1978; Harris & Mayr, 1975) that contain the same underlying physical mechanisms as the MCD (see, e.g., González-Galindo, Forget, Lápez-Valverde, Angelats i Coll, & Millour, 2009), and which can provide some relevant insights. Mayr and Harris (1977) and Forbes (1978) solved the equations governing the behavior of solar tide-driven O, O_2, N_2, Ar, He, and H density variations in Earth's thermosphere. At Earth, the dominant constituent is N_2 below about 160–220 km, where it transitions to O which remains the dominant constituent up to the exobase (~400 at solar minimum). At Mars, the dominant constituent is CO_2 up to the exobase near 200 km, where N_2 densities can be comparable with those of CO_2.

Here we will consider an analogy between CO_2 (major constituent), Ar and N_2 (minor constituents) in Mars thermosphere, and O (major constituent), Ar and He (minor constituents) in Earth's thermosphere, with primary emphasis on the CO_2-N_2 and O-He relationships. All of the following applies to equatorial latitudes. Moreover, we view 400 km at Earth and 200 km at Mars as analogous in terms of being just below the exobase during solar minimum conditions. For Earth, Mayr and Harris (1977) identify two processes as primarily responsible for tidal variations in O, Ar, and He: thermal expansion in diffusive equilibrium (dependent on temperature) and "wind-induced diffusion" (WID). WID refers to the momentum transfer between atmospheric constituents induced by the vertical velocity arising from divergence of the horizontal velocity field (e.g., see Harris & Mayr, 1975, where the relevant equations are also displayed.) WID modifies the diffusion that already exists

between a minor constituent (Ar and He) and the major constituent, O. The relative importance of these processes varies with height. Since O is a minor constituent below ∼170 km, it is affected by both processes; WID dominates below 240 km while thermal expansion dominates above 240 km. O variability due to WID has a phase (LST of maximum) of 0800, while the phase associated with thermal expansion shifts abruptly from 0400 below 200 km to ∼1600 at higher altitudes. Consequently the phase of O varies with height from ∼0600 at 140 km to almost 1600 at 400 km, the time of maximum of the exospheric temperature. The amplitude of the O relative perturbation at 400 km is 50%. For He, WID dominates over most of the thermosphere, but the thermal expansion contribution (with phase of 1600 LST) to the total 20% response at 400 km is about 14%. Yet, the phase of the total He response at 400 km is 0800, which reflects the dominance of WID at lower heights. For Ar, thermal expansion dominates above 200 km, and the effects of WID are small (∼20%) below 200 km, and shift the phase to later LSTs. At 400 km the amplitude and phase of Ar are 140% and 1600 LST. The interested reader may wish to refer to Figure S9 in Supporting Information S1, taken from Mayr and Harris (1977), which summarizes much of the above and more.

In summary, at Earth the effects of WID (thermal expansion) are more (less) important for species lighter (heavier) than the major constituent (O), and lead to respectively smaller (larger) amplitudes and shifts of phase to earlier (later) local times. And, the amplitudes and phases at 400 km are dependent on the relative contributions of thermal expansion and WID at lower heights. In the MCD results for DW1 depicted in Figure 3, the N_2 density response at 180 km is about 30% of that of CO_2 and shifted 2 hr earlier. This is broadly consistent with the presence of WID effects at Earth. The molecular weight of N_2 (28) is 64% of that of CO_2 (44). At Earth, the He response is 40% of that of O, 28% of which is connected with thermal expansion, but the molecular weight of He (4) is only 25% that of O (16); yet, the phase of He strongly reflects the influence of WID. It is reasonable to conclude that both thermal expansion and WID are playing a role in determining the DW1 response of N_2 at Mars. The smaller amplitude of the N_2 response relative to CO_2 (as compared with the O-He comparison at Earth) furthermore suggests that the WID influence is relatively larger than at Earth, although the smaller shift in phase relative to the major constituent is more modest than at Earth. Just as thermal equilibrium emerges as the major contributor to He variability at 400 km at Earth while the phase reflects the influence of WID at lower altitudes, a reverse argument may explain the smaller than expected phase shift of N_2 given the apparently larger influence of WID on its amplitude.

As an aside, referring back to Equation 5 (i.e., Equation 12 from Dudis and Reber (1976)), that equation neglects both thermal expansion and diffusion. Rather, it represents the local perturbation in a minor constituent density due directly to vertical winds, moreover applicable only to the range of horizontal scales and periods appropriate to large-scale GWs as opposed to tides.

We now turn to the interpretation of the MAVEN DW1 responses in Figure 3. We have verified that the 1200 LST phase of DW1 for CO_2 is the same as that of temperature in the MCD, consistent with expectations that thermal expansion in diffusive equilibrium is the dominant process determining the amplitude and phase of CO_2 in the MCD. However, it is clear that the amplitudes of the Ar and N_2 responses are smaller relative to CO_2 than is the case for MAVEN. Based on the above discussion, we conclude that the effects of WID relative to thermal expansion are overestimated in the MCD. Then there is the issue that the CO_2 phases occur roughly 4 hr later in the day (∼1600) in the observations than in the MCD (∼1200), while in both cases the solar heating maximizes at noon. At Earth, it has been known for a long time (e.g., Dickinson & Geisler, 1968) that the ∼1600 LST maximum in thermosphere density relative to the noon maximum in heating is due to a relatively large diurnally-varying adiabatic heating/cooling term in the thermal equation. The adiabatic term is due to vertical motions arising from divergence of the tidal horizontal wind field:

$$\frac{\partial T'}{\partial t} = \frac{J'}{c_p} - w'_D\Gamma + \quad \ldots \tag{6}$$

where T' is the temperature, J' represent tidal heating due to solar radiation absorption, c_p is the specific heat at constant pressure, w'_D is the component of vertical velocity associated with tidal horizontal wind divergence and the conservation of mass (apart from the *barometric* component due to thermal expansion), $\Gamma = \partial\overline{T}/\partial z + g/c_p$ is the mean atmospheric stability, and $\overline{T}$ is the DZM temperature. The adiabatic term in Equation 6 was referred to as the "missing heat source" in the early terrestrial literature, prior to that of Dickinson and Geisler (1968). It is

as important as EUV heating, and accounts for much of the observed time shift of the temperature maximum to late afternoon with respect to the noontime maximum in EUV heating.

The fact that a similar displacement between heating and density response exists in the MAVEN data suggests that this mechanism is operative in Mars thermosphere. And, moreover, that the absence of that displacement in the MCD suggests that the amplitude and/or phasing of adiabatic heating/cooling in the MCD warrants further investigation. It is also relevant to note that the Mars Global Ionosphere-Thermosphere Model (MGITM, Bougher et al., 2015) for solar minimum conditions does indicate a maximum temperature near LST = 1500 at 200 km, but a CO_2 density maximum near LST = 1200 hr (their Figure 2 and related text). This result is inconsistent with the above arguments pertaining to CO_2-temperature relative phasing, unless the CO_2 response reflects some influence of WID. And the 3-hr difference in the LST of maximum temperature between the MCD and MGITM remains to be explained.

Lastly, the "interference effects" in the htvslat structures of MCD DW1 and SW2 occurring between Ls = 180 and Ls = 330, and maximizing around Ls = 270 appear to be associated with the same dynamical drivers responsible for the so-called polar warming phenomenon in Mars thermosphere around 120 km (Bell et al., 2007; Bougher et al., 2006; González-Galindo, Forget, Lápez-Valverde, & Angelats i Coll, 2009; Wilson, 1997). These works are primarily confined to polar warming in the context of the DZM thermal and dynamical structure of Mars' thermosphere. As explained in the above works, the perihelion DZM global circulation pattern is one that consists of upwelling in the SH, inter-hemispheric flow from the SH to NH, and downwelling in the NH polar region. Similar to the arguments put forth in connection with Equation 6 in the upper thermosphere, the existence of large horizontal wind divergence, downwelling $\left(\overline{w}_D < 0\right)$, and adiabatic heating in the vicinity of 120 km in the winter polar regions is responsible for especially strong warming around Ls = 270 and a much reduced manifestation of this effect in the SH around Ls = 90.

As demonstrated by González-Galindo, Forget, Lápez-Valverde, and Angelats i Coll (2009), the strong DZM wind divergence responsible for the polar warming also contains a significant solar-synchronous LST variation, which is reflected in the MCD migrating tide depictions in the present work. A local time dependence connected with the polar warming was also alluded to by Wilson (1997) in connection with his reference to IRTM temperature measurements during polar warmings reported by Jakosky and Martin (1987). In the MCD this LST variation is manifested as temperature and density perturbations around perihelion that extend well equatorward of 48°S between 90 and 140 km in the WH, and that are in antiphase with similar but weaker ones in SH. Note, however, that the 48° latitude migrating tide values represent 48 ± 24° means, and thus include data extending poleward as far as 60° latitude. It is also notable that the LST variation of mesopause temperatures is out of phase in the MCD with respect to MAVEN Imaging Ultraviolet Spectrograph (IUVS) measurements, with the MCD showing maximum temperature in the nightside, while IUVS displays maximum temperatures around noon (Gupta et al., 2022). Some depictions of these responses for DW1 and related interpretive text are provided in Figures S10 and S11 of Supporting Information S1. Since these features are absent from the MAVEN results, we have not pursued investigation of the physics behind this phenomenon in the MCD. But this disparity does emphasize the value of the present work in terms of providing observational constraints for models seeking to emulate Mars dynamics and coupling with composition. To that point, the effects of energy and momentum deposition by non-orographic GWs are omitted in MCD version 5.3, which could play a role in this model-measurement disparity.

4. Summary and Conclusions

In this paper, we analyzed in-bound measurements of CO_2 densities, and inbound plus outbound measurements of Ar and N_2 densities, from MAVEN/NGIMS between 150 and 200 km altitude during 2015–2022 to reveal diurnal (DW1), semidiurnal (SW2) and terdiurnal (TW3) solar-synchronous tides in Mars thermosphere. These results were compared with complementary (similar-binned and averaged) results from the MCD. Well-established results from the terrestrial literature were employed to provide some qualitative insights into the MAVEN and MCD results, and their similarities and differences. In particular, Dickinson and Geisler (1968) first quantified the critical role of adiabatic heating and cooling due to the vertical wind field w'_D associated with tidal horizontal wind divergence (in contrast to vertical motions associated with thermal expansion) on the phase difference between exosphere temperature and upper-thermosphere density as revealed in satellite drag data of the era. Mayr and Harris (1977), Harris and Mayr (1975) and Forbes (1978) quantified the relative tidal amplitudes and phases of O, O_2, N_2, Ar, He, and H in Earth's thermosphere using linear models

specifically designed to explain various features of the first satellite-based mass spectrometer measurements of Earth's thermosphere. These works were especially important for quantifying the relative importance of thermal expansion and WID on the htvslat tidal structures of these constituents. Namely, that (a) the effects of WID (thermal expansion) are more (less) important for species lighter (heavier) than the major constituent, and lead to respectively smaller (larger) amplitudes and shifts of phase to earlier (later) local times; and (b) amplitudes and phases in the upper thermosphere are dependent on the relative contributions of thermal expansion and WID at lower heights.

The main conclusions of our study are summarized as follows:

1. Typical MAVEN amplitudes for DW1, SW2, and TW3 at Ls = 90 ± 60, Ls = 180 ± 60, Ls = 270 ± 60 between $\theta = \pm 48°$ at for example, 180 km are of order 90%–120%, 15%–20%, and $\lesssim$10% for CO_2 and Ar, and roughly 2/3 these values for N_2. Annual-mean amplitudes do not depart appreciably from these values, due to the phase coherence that accompanies solar-synchronous thermal forcing throughout the MY, combined with the absence of any consequential latitudinal structures between 48°S and 48°N. Uncertainties associated with these amplitudes are estimated to be of order 5%–6%.
2. MAVEN DW1 phases (LST of maxima) for CO_2, Ar and N_2 densities are consistently in the range 1400–1800 hr, suggesting the influence of large adiabatic heating/cooling contributions, phased so as to shift the density response from the solar heating maximum at noon. This interpretation is based on the analogous situation in Earth's thermosphere where the DW1 density response occurs near 1600 LST.
3. By analogy with studies for Earth's thermosphere, it is concluded that thermal expansion is the process most likely responsible for the DW1 responses of CO_2 and Ar in the MAVEN data, and that the influence of WID is reflected in the relatively smaller response of N_2. At the same time, the annual-mean upper thermosphere CO_2, Ar, and N_2 responses for MCD are of order 0.6, 0.6, and 0.35 those of MAVEN, suggesting that the effect of WID may be overestimated in the MCD as compared with MAVEN.
4. The absence of any vertical phase progressions attached to DW1 in the MAVEN data suggests predominantly in situ generation of this component. However, SW2 and TW3 phases, and in some cases amplitude structures, show evidence of contributions from components propagating upwards from below. It is not possible to quantify the relative contributions of in situ versus upward-propagating components based on the data alone. On the other hand, the MCD contains comparatively little evidence for vertical propagation from below in SW2 and TW3.
5. Between about Ls = 180 and Ls = 330, and maximizing around Ls = 270, MCD DW1, SW2, and TW3 htvslat amplitude structures are characterized by a marked interference pattern that arises from sources originating below and above about 150 km that are nearly in antiphase with each other. This effect is most acute for N_2, and even appears in the annual-mean for N_2, whereas this is not true for CO_2 and Ar. The response at higher altitudes in all cases is obviously of in situ origin, as is the case for the MAVEN responses. These effects are completely absent in the MAVEN data. Preliminary diagnosis of the MCD suggests that the lower-altitude response is connected with strong tidal wind divergences with origins akin to those responsible for winter polar warmings in the DZM, which appear to be exaggerated in the MCD. In fact, this out-of-phase relationship between upper and lower thermosphere temperatures is absent in IUVS temperature measurements (Gupta et al., 2022), supporting this diagnosis. A contributing factor to this measurement-model disparity may be the omission of non-orographic GWs in the MCD, which is currently under investigation.

As underscored by the last item listed above, the value and relevance of the present work is that it provides a new data source that can serve to validate and improve general circulation models of Mars thermosphere. It is anticipated that future investigations using the same data set will address solar-asynchronous tides and longitudinal structures in composition, zonally symmetric tides at high latitudes (±60–70°), and the diurnal and zonal mean composition of Mars thermosphere.

Data Availability Statement

The MAVEN data were obtained from the Planetary Data System (https://atmos.nmsu.edu/PDS/data/PDS4/MAVEN/ngims_bundle/). The MCD and related software are publicly available at http://www-mars.lmd.jussieu.fr.

Acknowledgments
This work was supported under award 80NSSC21K1101 from the NASA Mars Data Analysis Program to the University of Colorado, and under award 80GSFC21M0002 (MB). F.G.-G. acknowledges financial support from the grant CEX2021-001131-S funded by MCIN/AEI/10.13039/501100011033.

References

Bell, J. M., Bougher, S. W., & Murphy, J. R. (2007). Vertical dust mixing and the interannual variations in the Mars thermosphere. *Journal of Geophysical Research*, *112*(E12), E12002. https://doi.org/10.1029/2006JE002856

Benna, M., Mahaffy, P., Grebowsky, J., Fox, J. L., Yelle, R. V., & Jakosky, B. M. (2015). First measurements of composition and dynamics of the Martian ionosphere by MAVEN's neutral gas and ion mass spectrometer. *Geophysical Research Letters*, *42*(21), 8958–8965. https://doi.org/10.1002/2015GL066146

Bougher, S. W., Bell, J. M., Murphy, J. R., Lopez-Valverde, M. A., & Withers, P. G. (2006). Polar warming in the Mars thermosphere: Seasonal variations owing to changing insolation and dust distributions. *Geophysical Research Letters*, *33*(2), L02203. https://doi.org/10.1029/2005GL024059

Bougher, S. W., Pawlowski, D., Bell, J. M., Nelli, S., McDunn, T., Murphy, J. R., et al. (2015). Mars Global Ionosphere-Thermosphere Model (MGITM): Solar cycle, seasonal, and diurnal variations of the Mars upper atmosphere. *Journal of Geophysical Research: Planets*, *120*(2), 311–342. https://doi.org/10.1002/2014JE004715

Dickinson, R. E., & Geisler, J. E. (1968). Vertical motion field in the middle thermosphere from satellite drag densities. *Monthly Weather Review*, *96*(9), 606–616. https://doi.org/10.1175/1520-0493(1968)096<0606:VMFITM>2.0.CO;2

Dudis, J. J., & Reber, C. A. (1976). Composition effects in thermospheric gravity waves. *Geophysical Research Letters*, *3*(12), 727–730. https://doi.org/10.1029/GL003i012p00727

Emmert, J. T., Drob, D. P., Picone, J. M., Siskind, D. E., Jones, M., Jr., Mlynczak, M. G., et al. (2020). NRLMSIS 2.0: A whole atmosphere empirical model of temperature and neutral species densities. *Earth and Space Science*, *7*(3), e2020EA001321. https://doi.org/10.1029/2020EA001321

England, S. L., Liu, G., Kumar, A., Mahaffy, P. R., Elrod, M., Benna, M., et al. (2019). Atmospheric tides at high latitudes in the Martian upper atmosphere observed by MAVEN and MRO. *Journal of Geophysical Research: Space Physics*, *124*(4), 2943–2953. https://doi.org/10.1029/2019JA026601

England, S. L., Liu, G., Withers, P., Yiğit, E., Lo, D., Jain, S., et al. (2016). Simultaneous observations of atmospheric tides from combined in situ and remote observations at Mars from the MAVEN spacecraft. *Journal of Geophysical Research: Planets*, *121*(4), 594–607. https://doi.org/10.1002/2016JE004997

Fang, X., Forbes, J. M., Benna, M., Montabone, L., Curry, S., & Jakosky, B. (2022). The origins of long-term variability in Martian upper atmospheric densities. *Journal of Geophysical Research: Space Physics*, *127*(3), e2021JA030145. https://doi.org/10.1029/2021JA030145

Fang, X., Forbes, J. M., Gan, Q., Liu, G., Thaller, S., Bougher, S., et al. (2021). Tidal effects on the longitudinal structures of the Martian thermosphere and topside ionosphere observed by MAVEN. *Journal of Geophysical Research: Space Physics*, *126*(2), e2020JA028562. https://doi.org/10.1029/2020JA028562

Forbes, J. M. (1978). Tidal variations in thermospheric O, O_2, N_2, Ar, He, and H. *Journal of Geophysical Research*, *83*(A8), 3691–3698. https://doi.org/10.1029/JA083iA08p03691

Forbes, J. M., Lemoine, F. G., Bruinsma, S. L., Smith, M. D., & Zhang, X. (2008). Solar flux variability of Mars' exosphere densities and temperatures. *Geophysical Research Letters*, *35*(1), L01201. https://doi.org/10.1029/2007gl031904

Forbes, J. M., Zhang, X., Forget, F., Millour, E., & Kleinböhl, A. (2020). Solar tides in the middle and upper atmosphere of Mars. *Journal of Geophysical Research: Space Physics*, *125*(9), e2020JA028140. https://doi.org/10.1029/2020JA028140

Forget, F., Hourdin, F., Fournier, R., Hourdin, C., Talagrand, O., Collins, M., et al. (1999). Improved general circulation models of the Martian atmosphere from the surface to above 80 km. *Journal of Geophysical Research*, *104*(E10), 24155–24175. https://doi.org/10.1029/1999JE001025

Fu, M. H., Cui, J., Wu, X. S., Wu, Z. P., & Li, J. (2020). The variations of the Martian exobase altitude. *Earth and Planetary Physics*, *4*(1), 4–10. https://doi.org/10.26464/epp2020010

González-Galindo, F., Chaufray, J.-Y., López-Valverde, M. A., Gilli, G., Forget, F., Leblanc, F., et al. (2013). Three-dimensional Martian ionosphere model: I. The photochemical ionosphere below 180 km. *Journal of Geophysical Research: Planets*, *118*(10), 2105–2123. https://doi.org/10.1002/jgre.20150

González-Galindo, F., Forget, F., Lápez-Valverde, M. A., & Angelats i Coll, M. (2009). A ground-to-exosphere Martian general circulation model: 2. Atmosphere during solstice conditions—Thermospheric polar warming. *Journal of Geophysical Research*, *114*, E08004. https://doi.org/10.1029/2008JE003277

González-Galindo, F., Forget, F., Lápez-Valverde, M. A., Angelats i Coll, M., & Millour, E. (2009). A ground-to-exosphere Martian general circulation model: 1. Seasonal, diurnal, and solar cycle variation of thermospheric temperatures. *Journal of Geophysical Research*, *114*(E4), E04001. https://doi.org/10.1029/2008JE003246

González-Galindo, F., López-Valverde, M. A., Forget, F., García-Comas, M., Millour, E., & Montabone, L. (2015). Variability of the Martian thermosphere during eight Martian years as simulated by a ground-to-exosphere global circulation model. *Journal of Geophysical Research: Planets*, *120*(11), 2020–2035. https://doi.org/10.1002/2015JE004925

Gupta, S., Yelle, R. V., Schneider, N. M., Jain, S. K., González-Galindo, F., Verdier, L., et al. (2022). Thermal structure of the Martian upper mesosphere/lower thermosphere from MAVEN/IUVS stellar occultations. *Journal of Geophysical Research: Planets*, *127*(11), e2022JE007534. https://doi.org/10.1029/2022JE007534

Guzewich, S. D., Fedorova, A. A., Kahre, M. A., & Toigo, A. D. (2020). Studies of the 2018/Mars year 34 planet-encircling dust storm. *Journal of Geophysical Research: Planets*, *125*(12), e2020JE006700. https://doi.org/10.1029/2020JE006700

Harris, I., & Mayr, H. G. (1975). Diurnal variations in the thermosphere 1. Theoretical formulation. *Journal of Geophysical Research*, *80*(28), 3925–3933. https://doi.org/10.1029/JA080i028p03925

Hughes, J., Gasperini, F., & Forbes, J. M. (2022). Solar rotation effects in Martian thermospheric density as revealed by five years of MAVEN observations. *Journal of Geophysical Research: Planets*, *127*(1), e2021JE007036. https://doi.org/10.1029/2021JE007036

Jakosky, B. M., Grebowsky, J. M., Luhmann, J. G., & Brain, D. A. (2015). Initial results from the MAVEN mission to Mars. *Geophysical Research Letters*, *42*(21), 8791–8802. https://doi.org/10.1002/2015GL065271

Jakosky, B. M., & Martin, T. Z. (1987). Mars: North-polar atmospheric warming during dust storms. *Icarus*, *72*(3), 528–534. https://doi.org/10.1016/0019-1035(87)90050-9

Liu, G., England, S., Lillis, R. J., Mahaffy, P. R., Elrod, M., Benna, M., & Jakosky, B. (2017). Longitudinal structures in Mars' upper atmosphere as observed by MAVEN/NGIMS. *Journal of Geophysical Research: Space Physics*, *122*(1), 1258–1268. https://doi.org/10.1002/2016JA023455

Mahaffy, P. R., Benna, M., King, T., Harpold, D. N., Arvey, R., Barciniak, M., et al. (2015). The neutral gas and ion mass spectrometer on the Mars atmosphere and volatile evolution mission. *Space Science Reviews*, *195*(1–4), 49–73. https://doi.org/10.1007/s11214-014-0091-1

Mayr, H. G., & Harris, I. (1977). Diurnal variations in the thermosphere, 2. Temperature, composition, and winds. *Journal of Geophysical Research*, *82*(19), 2628–2640. https://doi.org/10.1029/JA082i019p02628

Millour, E., Forget, F., Spiga, A., Vals, M., Zakharov, V., Navarro, T., et al. (2018). The Mars Climate Database (Version 5.3). In *Scientific Workshop: From Mars Express to ExoMars, 27–28 February 2018, ESAC Madrid, Spain*.

Moudden, Y., & Forbes, J. M. (2008). Topographic connections with density waves in Mars' aerobraking regime. *Journal of Geophysical Research*, *113*(E11), E11009. https://doi.org/10.1029/2008JE003107

Moudden, Y., & Forbes, J. M. (2015). Density prediction in Mars' aerobraking region. *Space Weather*, *13*(1), 86–96. https://doi.org/10.1002/2014SW001121

Nair, H. (1996). *Photochemical processes in the atmospheres of Earth and Mars* (Ph.D. Dissertation). California Institute of Technology.

Nair, H., Allen, M., Anbar, A. D., Yung, Y. L., & Clancy, R. T. (1994). A photochemical model of the Martian atmosphere. *Icarus*, *111*(1), 124–150. https://doi.org/10.1006/icar.1994.1137

Oberheide, J., Forbes, J. M., Zhang, X., & Bruinsma, S. L. (2011). Climatology of upward propagating diurnal and semidiurnal tides in the thermosphere. *Journal of Geophysical Research*, *116*(A11), A11306. https://doi.org/10.1029/2011JA016784

Truskowski, A. O., Forbes, J. M., Zhang, X., & Palo, S. E. (2014). New perspectives on thermosphere tides: 1. Lower thermosphere spectra and seasonal-latitudinal structures. *Earth Planets and Space*, *66*, 136. https://doi.org/10.1186/s40623-014-0136-4

Wilson, R. J. (1997). A general circulation model of the Martian polar warming. *Geophysical Research Letters*, *24*(2), 123–126. https://doi.org/10.1029/96GL03814

Withers, P. G., Bougher, S. W., & Keating, G. M. (2003). The effects of topographically controlled thermal tides in the Martian upper atmosphere as seen by the MGS accelerometer. *Icarus*, *164*(1), 14–32. https://doi.org/10.1016/s0019-1035(03)00135-0

Wu, Z., Li, T., & Dou, X. (2015). Seasonal variation of Martian middle atmosphere tides observed by the Mars Climate Sounder. *Journal of Geophysical Research: Planets*, *120*(12), 2206–2223. https://doi.org/10.1002/2015JE004922